galaxies[20], 50 times as much H_2 would be required to fit the rotation curve. □

Received 18 June; accepted 21 September 2004; doi:10.1038/nature03054.

1. Casertano, S. & van Gorkom, J. H. Declining rotation curves—the end of a conspiracy? *Astron. J.* **101,** 1231–1241 (1991).
2. Young, J. S. & Scoville, N. Z. Molecular gas in galaxies. *Annu. Rev. Astron. Astrophys.* **29,** 581–625 (1991).
3. Combes, F. Distribution of CO in the Milky Way. *Annu. Rev. Astron. Astrophys.* **29,** 195–237 (1991).
4. Braine, J. *et al.* A CO(1-0) and CO(2-1) survey of nearby spiral galaxies. I—Data and observations. *Astron. Astrophys. Suppl.* **97,** 887–936 (1993).
5. Thornley, M. D. Uncovering spiral structure in flocculent galaxies. *Astrophys. J.* **469,** L45–L48 (1996).
6. Digel, S., de Geus, E. & Thaddeus, P. Molecular clouds in the extreme outer galaxy. *Astrophys. J.* **422,** 92–101 (1994).
7. Braine, J., Brouillet, N. & Baudry, A. The anatomy of an isolated spiral galaxy: NGC 4414. *Astron. Astrophys.* **318,** 19–28 (1997).
8. Cuillandre, J., Lequeux, J., Allen, R. J., Mellier, Y. & Bertin, E. Gas, dust, and young stars in the outer disk of M31. *Astrophys. J.* **554,** 190–201 (2001).
9. van Zee, L., Salzer, J. J., Haynes, M. P., O'Donoghue, A. A. & Balonek, T. J. Spectroscopy of outlying H II regions in spiral galaxies: abundances and radial gradients. *Astron. J.* **116,** 2805–2833 (1998).
10. Engargiola, G., Plambeck, R. L., Rosolowsky, E. & Blitz, L. Giant molecular clouds in M33. I. BIMA all-disk survey. *Astrophys. J. Suppl.* **149,** 343–363 (2003).
11. Heyer, M. H. & Terebey, S. The anatomy of the Perseus spiral arm: 12CO IRAS imaging observations of the W3-W4-W5 cloud complex. *Astrophys. J.* **502,** 265–277 (1998).
12. Blitz, L., Spergel, D. N., Teuben, P. J., Hartmann, D. & Burton, W. B. High-velocity clouds: building blocks of the local group. *Astrophys. J.* **514,** 818–843 (1999).
13. Dickman, R. L., Snell, R. L. & Schloerb, F. P. Carbon monoxide as an extragalactic mass tracer. *Astrophys. J.* **309,** 326–330 (1986).
14. Sodroski, T. J. *et al.* A three-dimensional decomposition of the infrared emission from dust in the Milky Way. *Astrophys. J.* **480,** 173–187 (1997).
15. Spitzer, L. *Physical Processes in the Interstellar Medium* 333 (Wiley-Interscience, New York, 1978).
16. Dickey, J. M. & Brinks, E. An H I absorption survey of M31 and M33—The mixture of warm and cool phases in the interstellar media of spiral galaxies. *Astrophys. J.* **405,** 153–162 (1993).
17. Braun, R. The temperature and opacity of atomic hydrogen in spiral galaxies. *Astrophys. J.* **484,** 637–655 (1997).
18. Pogge, R. W. Ionized gas in the nuclear regions of nearby non-Seyfert spiral galaxies. *Astrophys. J. Suppl.* **71,** 433–453 (1989).
19. Braine, J., Combes, F. & van Driel, W. NGC 4414: A flocculent galaxy with a high gas surface density. *Astron. Astrophys.* **280,** 451–467 (1993).
20. Pfenniger, D. & Combes, F. Is dark matter in spiral galaxies cold gas? Fractal models and star non-formation. *Astron. Astrophys.* **285,** 94–118 (1994).

Acknowledgements We thank J.-C. Cuillandre for taking the CFHT image and T. Osterloo, G. Gentile and G. Jozsa for making the H I data available. This work is based on observations carried out with the IRAM 30-m telescope. IRAM is supported by INSU/CNRS (France), MPG (Germany), and IGN (Spain).

Competing interests statement The authors declare that they have no competing financial interests.

Correspondence or requests for materials should be addressed to J.B. (braine@obs.u-bordeaux1.fr).

Electrical generation and absorption of phonons in carbon nanotubes

B. J. LeRoy, S. G. Lemay, J. Kong & C. Dekker

Kavli Institute of Nanoscience, Delft University of Technology, Lorentzweg 1, 2628 CJ, Delft, The Netherlands

The interplay between discrete vibrational and electronic degrees of freedom directly influences the chemical and physical properties of molecular systems. This coupling is typically studied through optical methods such as fluorescence, absorption and Raman spectroscopy. Molecular electronic devices provide new opportunities for exploring vibration–electronic interactions at the single molecule level[1–6]. For example, electrons injected from a scanning tunnelling microscope tip into a metal can excite vibrational excitations of a molecule situated in the gap between tip and metal[7]. Here we show how current directly injected into a freely suspended individual single-wall carbon nanotube can be used to excite, detect and control a specific vibrational mode of the molecule. Electrons tunnelling inelastically into the nanotube cause a non-equilibrium occupation of the radial breathing mode, leading to both stimulated emission and absorption of phonons by successive electron tunnelling events. We exploit this effect to measure a phonon lifetime of the order of 10 ns, corresponding to a quality factor of well over 10,000 for this nanomechanical oscillator.

Single-wall carbon nanotubes (SWCNTs) were grown by chemical vapour deposition on a Pt substrate, which had predefined 100-nm-wide trenches etched in it. The SWCNTs were measured as-grown without any further processing. Details of the preparation of the samples used in this experiment have been reported previously[8]. Figure 1a sketches the set-up for the measurements indicating the scanning tunnelling microscope (STM) tip and the SWCNT crossing a trench. Figure 1b shows an STM topographic image of a nanotube suspended across a trench. The SWCNT is suspended over a distance of about 100 nm. Figure 1c is a zoom-in on the tube in the region over the trench, demonstrating atomic resolution.

An STM can reveal information about electronic structure with high spatial resolution through tunnelling spectroscopy. Figure 2a plots the normalized tunnelling differential conductance, $(dI/dV)/(I/V)$, as a function of sample voltage near the edge of a trench for the semiconducting SWCNT of Fig. 1b. As the sample voltage is decreased, a series of sharp spikes are obtained owing to the Coulomb staircase[8,9]. The spacing between peaks is a measure of the energy necessary to add an electron to the SWCNT. Figure 2b plots the normalized differential conductance at the centre of the trench. New side peaks appear in addition to the previously observed Coulomb peaks. Such additional peaks in the differential conductance can occur when there are new channels through which electrons can tunnel onto the SWCNT. Figure 2c shows the full spatial dependence of the tunnelling differential conductance. The four main Coulomb staircase peaks shift in energy owing to a changing tip–SWCNT capacitance[8] but persist throughout the image. In contrast, the additional side peaks are localized in the part of the SWCNT that is suspended. That side peaks only occur in the suspended portion explains why they have not been observed in previous STM measurements where nanotubes are lying on a conducting surface.

An STM allows the resistance of one of the tunnel barriers to be changed, thus controlling the current through the SWCNT at a fixed

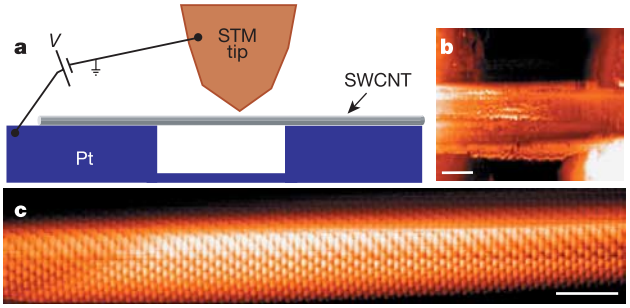

Figure 1 Measurement set-up and topographic images. **a**, Schematic diagram showing the set-up for performing spectroscopy on suspended SWCNTs. A voltage is applied to the substrate with respect to the tip, and the current flowing from the substrate through the SWCNT to the tip is measured. **b**, STM image of a nanotube crossing a trench. Scale bar, 25 nm. The apparent width of the 2-nm-diameter tube is enlarged by tip convolution. **c**, High-resolution image of the suspended portion of the SWCNT showing atomic resolution. Scale bar, 2 nm. The STM images were taken with a feedback current of 300 pA at −1 V. All of the measurements were performed at 5 K in an ultrahigh-vacuum STM.

applied voltage. On the basis of previous transport measurements, the resistance of the SWCNT–substrate barrier is known to be in the range 10–1,000 kΩ. Since the resistance of the tip–SWCNT barrier (~1 GΩ) is much greater than the SWCNT–substrate barrier, the total resistance and tunnel rate is set by the former barrier. Figure 3a plots the normalized differential conductance through a metallic SWCNT as a function of bias voltage for a low setpoint current, $I_{set} = 100$ pA, and a sample voltage of −0.6 V. The peaks due to the Coulomb staircase appear in groups of four, indicating that there are two spin-degenerate bands in this metallic SWCNT (refs 10 and 11, and S. Sapmaz, manuscript in preparation). Figure 3b and c plots the differential conductance with a medium setpoint current of 300 pA and a high current of 1,000 pA, respectively. Many additional peaks have appeared on either side of the main Coulomb staircase peaks. The peaks are equally spaced in energy on both sides of the main Coulomb peaks. Although the side-peak intensities change, the energy relative to the Coulomb peak is found to be independent of the current.

We attribute these side peaks to phonon-assisted tunnelling into the SWCNT. By absorbing or emitting a phonon, electrons tunnelling onto the SWCNT can increase or decrease their energy by $\hbar\omega$, where ω is the frequency of the phonon. Side peaks thus appear at energies $\hbar\omega$ from the main Coulomb peaks. Figure 3d is a zoom-in on one of the Coulomb peaks showing side peaks corresponding to both emission and absorption of a phonon, in direct analogy to the well-known Stokes and anti-Stokes peaks in Raman spectroscopy. The main Coulomb peak occurs when electrons tunnel elastically from the STM tip to the SWCNT (Fig. 3f). Peaks at energies above the Coulomb peaks (farther from $V = 0$) are due to electrons emitting a phonon when tunnelling (Fig. 3e). Likewise, side peaks on the low-energy side of the Coulomb peaks (closer to $V = 0$) correspond to electrons absorbing a phonon from the SWCNT when tunnelling (Fig. 3g). Note that the observation of a strong peak for phonon absorption is very surprising given the fact that at equilibrium, without current, the population of phonons is extremely small at the low temperatures (5 K) of our experiment. The appearance of such peaks implies that current through the SWCNT induces a non-equilibrium phonon distribution. The phonon absorption effect has not previously been observed in electrical transport measurements. The non-equilibrium phonon distribution is furthermore responsible for the enhancement of the peaks on the high-energy side through stimulated emission.

It is possible to identify the specific phonon mode that we study in this experiment. For the 2.5-nm-diameter SWCNT of Fig. 2, the energy is found to be $E = 11.8 \pm 1.4$ meV, which corresponds to the

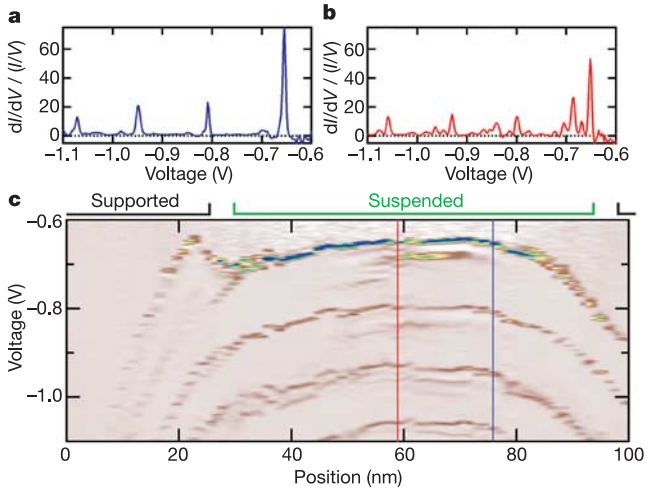

Figure 2 Spatially resolved spectroscopy along the suspended semiconducting SWCNT shown in Fig. 1b. **a**, Spectroscopy along the blue line in **c**, showing four spikes associated with the Coulomb staircase. The Coulomb staircase behaviour is determined by the two capacitances and resistances; the tip–SWCNT, and the SWCNT–substrate. The peaks occur when the Fermi level of the substrate aligns with states in the conduction band of the SWCNT. **b**, Spectroscopy along the red line in **c**, showing side peaks in addition to the Coulomb staircase peaks. **c**, Plot of the normalized differential conductance (colour scale) as a function of voltage and position. Sharp spikes are visible at all positions due to the Coulomb staircase, while extra peaks are visible only in the centre of the suspended region. The differential conductance was measured using lock-in detection with a 2 mV r.m.s. excitation voltage. The setpoint current was 300 pA at −1.25 V. The coloured lines above **c** indicate the regions where the SWCNT is supported (black) and suspended (green).

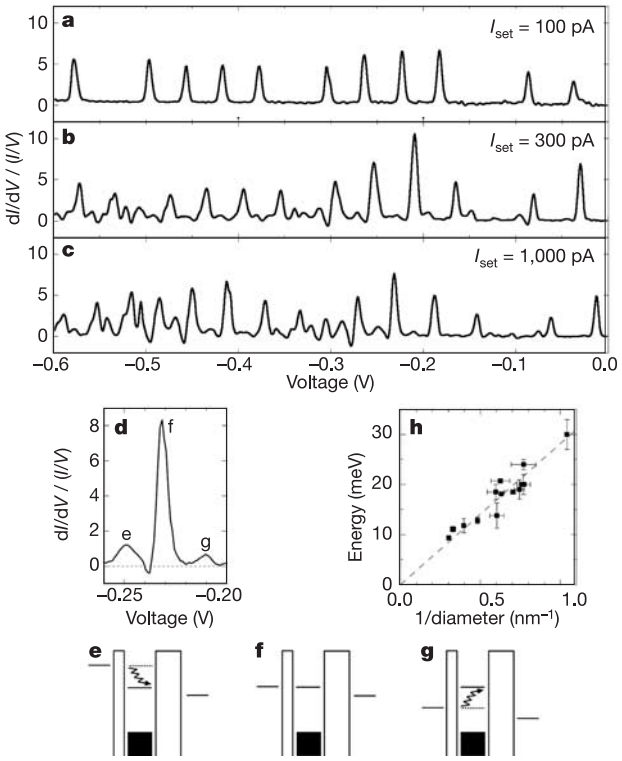

Figure 3 Current and diameter dependence of phonon-assisted tunnelling. **a**, Normalized differential conductance of a metallic SWCNT as a function of sample voltage taken with a low setpoint current I_{set} at −0.6 V. The tip is located at the centre of the suspended SWCNT. A series of sharp peaks is visible due to the Coulomb staircase as the Fermi level of the substrate aligns with unoccupied states of the SWCNT. **b**,**c**, Same as **a** with increasing setpoint current. A series of side peaks has appeared near the main Coulomb staircase peaks due to absorption and emission of phonons. To convert from sample voltage to energy, the capacitances between the tip and SWCNT, and the SWCNT and substrate must be known. The voltage dropped across the substrate–SWCNT junction is the applied voltage times the ratio of the tip–SWCNT capacitance and the total capacitance. These capacitances were determined from the spacing of the Coulomb peaks and the conductance between peaks[8,19]. **d**, Zoom-in on one of the peaks showing side peaks corresponding to the emission (E) and absorption (G) of phonons. The data show a negative differential resistance between the main peak and the emission peak, which is often observed in these experiments. **e**, Energy diagram for emission of a single phonon showing that an increased energy is needed for electron tunnelling. The distance between the solid black line and the top of the black box represents the Coulomb charging energy. **f**, Energy diagram for elastic tunnelling where a level in the SWCNT is aligned with the leads. **g**, Energy diagram for absorption of a phonon, which decreases the energy needed for tunnelling. **h**, Plot of the energy of the side peaks as a function of inverse diameter, showing a linear relationship. The horizontal error bars arise from the width of the van Hove singularities, while the vertical error bars are the standard deviation of the side-peak energy. The dashed line is the expected energy for the radial breathing mode obtained from ref. 13, and is plotted without any adjustable parameters.

energy of the radial breathing mode (RBM). To verify the origin of the side peaks as the RBM phonon, we have repeated these measurements for a series of metallic and semiconducting SWCNTs. The measured energy of the side peaks as a function of inverse SWCNT diameter is plotted in Fig. 3h. The diameter of the SWCNTs is determined from the spacing of the first van Hove singularities[12]. The dashed line is the theoretical energy dependence of the RBM, $27.8/d$ meV, where d is the diameter of the SWCNT in nm (ref. 13). The measured data points are best fitted with the equation $28.1 \pm 0.8\,\text{meV}/d$, which agrees very well with theory as well as with previously obtained results using Raman spectroscopy[13]. This demonstrates that the dominant phonon mode excited by electrons tunnelling into the SWCNT is the RBM, in agreement with other recent observations[14]. Electrons that tunnel into the SWCNT move at the Fermi velocity, thus travelling 10 nm in ~10 fs while the period of the RBM oscillation is ~370 fs. This suggests that circumferentially symmetric and low-k values of phonons are preferentially excited. This explains why the RBM is observed while the many other modes in the phonon density of states are not. When considering the excitation of low-k phonons and bending modes, we can exclude acoustic phonons as these will not be observed because of their low energy.

The new peaks that are observed for increased values of the current allow us to estimate the lifetime of the phonon in an individual SWCNT. The fact that side peaks on the low-energy side are visible only for faster rates of electron tunnelling implies that the decay time for the phonon mode in this SWCNT is longer than the average time between electron tunnelling events at these rates. For example, for the case of Fig. 3b, the current for the first absorption peak visible at −0.15 V gives an average rate of electron tunnelling events of $1.44 \times 10^8\,\text{s}^{-1}$. This gives a decay time of at least $\tau \approx 7$ ns, which is more than 50 times longer than observed in Raman experiments on bundles of SWCNTs[15]. The decay time in the Raman data may be caused by coupling to other SWCNTs or the substrate which are absent in our case. Our measured decay time corresponds to a lower bound for the quality factor $Q = \tau E/h$ of 20,000 for the RBM. Typical values of Q that we obtain for the RBM in our devices are in the range 5,000–30,000. These large Q values are an order of magnitude larger than previous reports for other phonon modes in SWCNTs[16], and are of the same order as those found in lithographically fabricated nanomechanical oscillators[17].

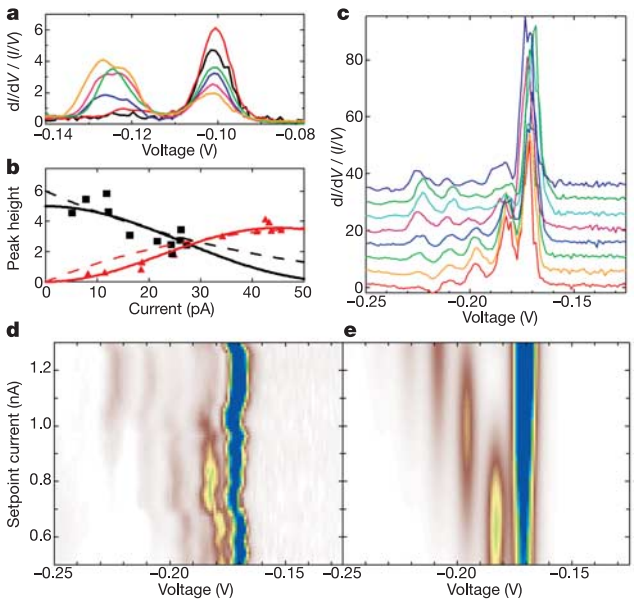

Figure 4 Comparison of the observed current dependence with theory. **a**, Normalized differential conductance versus bias voltage for a series of different currents ranging from 5 to 50 pA. As the current is increased, the main peak at −0.10 V decreases while the side peak at −0.125 V, associated with emission of a phonon, increases. **b**, Strength of the main (black squares) and first side peak (red triangles) as a function of the current at the given peak along with a fit using Bessel functions as described in the text. Dashed lines are for the perturbation $\alpha = \sqrt{I/\gamma}$ with $\gamma = 20$ pA, while solid lines are for $\alpha = I/\beta$ with $\beta = 24.5$ pA. **c**, Differential conductance as a function of bias voltage for a series of increasing currents from 500 to 1,300 pA, for a different SWCNT to **a**. **d**, Experimentally measured dependence of the differential conductance on current showing additional side peaks appearing as the current is increased. **e**, Simulation of the effect of increasing the current using $\alpha = I/\beta$ with $\beta = 310$ pA, which changes the phonon population and allows multiple phonon excitations. The conductance for the nth peak is given by the square of the nth-order Bessel function of the first kind. The data for **d** and **e** concern the first peak of a semiconducting SWCNT with zero current in the gap, and therefore there are no side peaks associated with phonon absorption (that is, on the right side of the main peak).

To further quantify the effect of the tunnelling current on the vibrational excitations of the SWCNT, we have compared the measured differential conductance as a function of current with a simple model of phonon-assisted tunnelling. Figure 4a shows a specific differential-conductance peak as a function of voltage for a series of different currents. As the current is increased, the strength of the main Coulomb peak decreases whereas the peak associated with phonon emission increases. This shows that the probability of emitting a phonon is controlled by the rate of electrons passing through the SWCNT. The amplitude of these two peaks as a function of current is plotted in Fig. 4b, showing the side peak becoming stronger than the main peak. Figure 4c and d plots the differential conductance as a function of voltage and current for a different SWCNT. As the current is increased, an increasing number of side peaks (up to 4) appears. This shows that multi-phonon excitations become possible at high current levels.

In analogy to photon-assisted tunnelling, we can model the effect of the phonons as an oscillating potential on the SWCNT proportional to $\alpha\cos(\omega t)$, where α is the strength of the perturbation and ω is the frequency of the phonon mode[18]. This model predicts that the Coulomb peak at energy ε_0 evolves into a series of peaks $\sum_n J_n^2(\alpha)\frac{\partial f}{\partial V}(eV - \varepsilon_0 - n\hbar\omega)$, where f is the Fermi function, J_n is the nth order Bessel function of the first kind, and n labels the peak number. The electron–phonon coupling term in the hamiltonian is linear in the phonon annihilation and creation operators, and therefore the strength of the perturbation $\alpha \propto \sqrt{N}$, where N is the number of phonons. Because the tunnel current I excites the phonons, a simple estimate is that $N \propto I$ and therefore $\alpha = \sqrt{I/\gamma}$, where γ is an unknown fitting parameter. The dashed lines in Fig. 4b show the expected peak height for the main peak and the first excited state as a function of current using this model. This simple model captures the essential trends in the experimental results. A better quantitative agreement to the experimental results can be obtained, however, if we assume that $N \propto I^2$. This gives a perturbation that is linear in the current, $\alpha = I/\beta$, where β is an unknown fitting parameter. The results of the simulations using this relationship for α are shown by the solid lines in Fig. 4b and e. An excellent agreement is obtained with only two largely uncorrelated fitting parameters, the peak height at zero current and β. As the current is increased in both the experimental data and the simulations, the number and strength of side peaks associated with phonon-assisted tunnelling increase, indicating that it is possible to control the population of phonons excited in a SWCNT.

Summing up, we have demonstrated that electrons passing through an individual carbon nanotube can populate phonon modes of the nanotube. This distribution can be probed with tunnelling spectroscopy that shows that electrons can both absorb and emit phonons when tunnelling onto the SWCNT. More theoretical work is needed to understand the current dependence of the phonon-assisted tunnelling peaks. These new phenomena

allow the measurement of long phonon lifetimes and high quality factors. Furthermore, it opens the door to the design of experiments with a known and controlled phonon population. □

Received 7 June; accepted 20 September 2004; doi:10.1038/nature03046.

1. Park, H. *et al.* Nanomechanical oscillations in a single-C_{60} transistor. *Nature* **407,** 57–60 (2000).
2. Pasupathy, A. N. *et al.* Vibration-assisted electron tunneling in C_{140} single-molecule transistors. Preprint at ⟨http://arxiv.org/cond-mat/0311150⟩ (2003).
3. Park, J. *et al.* Coulomb blockade and the Kondo effect in single-atom transistors. *Nature* **417,** 722–725 (2002).
4. Zhitenev, N. B., Meng, H. & Bao, Z. Conductance of small molecular junctions. *Phys. Rev. Lett.* **88,** 226801 (2002).
5. Qiu, X. H., Nazin, G. V. & Ho, W. Vibronic states in single molecule electron transport. *Phys. Rev. Lett.* **92,** 206102 (2004).
6. Weig, E. M. *et al.* Single-electron-phonon interaction in a suspended quantum dot phonon cavity. *Phys. Rev. Lett.* **92,** 046804 (2004).
7. Stipe, B. C., Rezaei, M. A. & Ho, W. Single-molecule vibrational spectroscopy and microscopy. *Science* **280,** 1732–1735 (1998).
8. LeRoy, B. J., Lemay, S. G., Kong, J. & Dekker, C. Scanning tunneling spectroscopy of suspended single-wall carbon nanotubes. *Appl. Phys. Lett.* **84,** 4280–4282 (2004).
9. Grabert, H. & Devoret, M. H. *Single Charge Tunneling* (Plenum, New York, 1992).
10. Liang, W. J., Bockrath, M. & Park, H. Shell filling and exchange coupling in metallic single-walled carbon nanotubes. *Phys. Rev. Lett.* **88,** 126801 (2002).
11. Cobden, D. H. & Nygard, J. Shell filling in closed single-wall carbon nanotube quantum dots. *Phys. Rev. Lett.* **89,** 046803 (2002).
12. Venema, L. C., Meunier, V., Lambin, Ph. & Dekker, C. Atomic structure of carbon nanotubes from scanning tunneling microscopy. *Phys. Rev. B* **61,** 2991–2996 (2000).
13. Dresselhaus, M. S. & Eklund, P. C. Phonons in carbon nanotubes. *Adv. Phys.* **49,** 705–814 (2000).
14. Vitali, L. *et al.* Phonon spectromicroscopy of carbon nanostructures with atomic resolution. *Phys. Rev. Lett.* **93,** 136103 (2004).
15. Iliev, M. N., Litvinchuk, A. P., Arepalli, S., Nikolaev, P. & Scott, C. D. Fine structure of the low-frequency Raman phonon bands of single-wall carbon nanotubes. *Chem. Phys. Lett.* **316,** 217–221 (2000).
16. Reulet, B. *et al.* Acoustoelectric effects in carbon nanotubes. *Phys. Rev. Lett.* **85,** 2829–2832 (2000).
17. Cleland, A. *Foundations of Nanomechanics* (Springer, Berlin, 2003).
18. Tien, P. K. & Gordon, J. P. Multiphoton process observed in the interaction of microwave fields with the tunneling between superconductor films. *Phys. Rev.* **129,** 647–651 (1963).
19. Hanna, A. E. & Tinkham, M. Variation of the Coulomb staircase in a two-junction system by fractional electron charge. *Phys. Rev. B* **44,** 5919–5922 (1991).

Acknowledgements We thank Ya. M. Blanter for discussions, and NWO and FOM for funding.

Competing interests statement The authors declare that they have no competing financial interests.

Correspondence and requests for materials should be addressed to C.D. (dekker@mb.tn.tudelft.nl).

Random quasi-phase-matching in bulk polycrystalline isotropic nonlinear materials

M. Baudrier-Raybaut[1], R. Haïdar[1], Ph. Kupecek[1,2], Ph. Lemasson[3] & E. Rosencher[1,4]

[1]*DMPH and DOTA/ONERA, Office National d'Etudes et de Recherches Aérospatiales, Chemin de la Hunière, 91761 Palaiseau, France*
[2]*Université Pierre et Marie Curie, 5 Place Jussieu, Paris 75005, France*
[3]*LPSC/CNRS, 1 Place Aristide Briand, F-92195, France*
[4]*Département de Physique, Ecole Polytechnique, 91228 Palaiseau, France*

Three-wave mixing in nonlinear materials—the interaction of two light waves to produce a third—is a convenient way of generating new optical frequencies from common laser sources. However, the resulting optical conversion yield is generally poor, because the relative phases of the three interacting waves change continuously as they propagate through the material[1]. This phenomenon, known as phase mismatch, is a consequence of optical dispersion (wave velocity is frequency dependent), and is responsible for the poor optical conversion potential of isotropic nonlinear materials[2]. Here we show that exploiting the random motion of the relative phases in highly transparent polycrystalline materials can be an effective strategy for achieving efficient phase matching in isotropic materials. Distinctive features of this 'random quasi-phase-matching' approach are a linear dependence of the conversion yield with sample thickness (predicted in ref. 3), the absence of the need for either preferential materials orientation or specific polarization selection rules, and the existence of a wavelength-dependent resonant size for the polycrystalline grains.

Much effort has recently been devoted to the development of materials which are suitable for nonlinear optical frequency conversion from the near- to the mid-infrared regions[4–7]. Many semiconductor (GaAs, ZnSe, …) materials of space group $\bar{4}3m$ are excellent candidates: they are widespread and mature optoelectronics graded materials, they are transparent in the mid-infrared and they display particularly high nonlinear 2nd-order susceptibilities (that is, for three-wave interaction). In single-crystalline materials, the main factor for an efficient optical conversion is the coherence length Λ_c, the distance over which the relative phase lag of the three waves add up to π. Indeed, because of the different relative phase velocities between the three interacting waves, optical power flows back and forth from the converted waves towards the pumping waves (that is, backconversion) as soon as the interacting distance becomes larger than the coherence length (see Fig. 1). Phase-matching is thus obtained when the coherence length is much longer than the interaction distance in the material. Because of the lack of optical birefringence, such a situation cannot be obtained naturally in isotropic $\bar{4}3m$ semiconductors over long distance. Instead, so-called quasi-phase-matching scenarios based on epitaxial growth on patterned substrates need to be developed[1,8–10].

The backconversion process results from an interference effect between the three coherent waves. Such interference could be destroyed if the waves were allowed to lose their respective phases randomly in the material, in that the nonlinear susceptibility does not average to zero. Such parametric interactions in disordered media have attracted considerable attention in recent years, with a particular emphasis on the nonlinear diffusion/scattering processes[11–14]: In these studies, the average size of the nanocrystal-

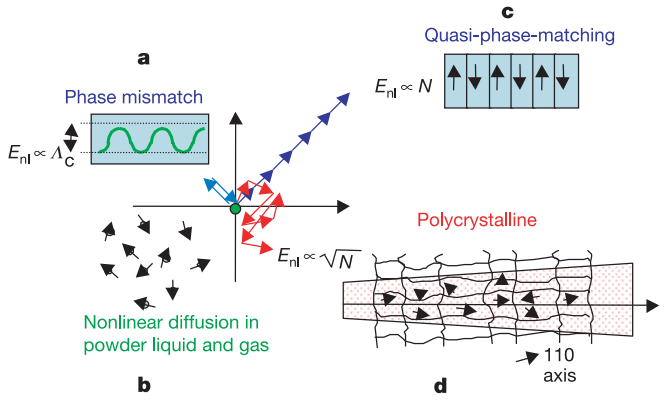

Figure 1 Three-wave mixing mechanisms in bulk, powder, periodically poled and polycrystalline materials. In bulk nonlinear optical materials, the relative phase of the three interacting fields grows continuously with the propagating distance, gaining a phase lag of π every coherence length Λ_c. The transfer of energy between the waves thus oscillates with a period of $2\Lambda_c$, leading to a small (if not null) conversion efficiency (**a**). In quasi-phase-matched materials[10], the orientation of the crystal is rotated every Λ_c, compensating the phase lag of π so that the energy transfer E_{nl} adds up constructively with the propagating distance ($E_{nl} \propto N$, where N is the number of grains) (**c**). In a totally disordered material (powder, gas, liquid), each particle behaves independently, scattering the nonlinearly generated fields in an incoherent way (**b**). In polycrystalline materials, the relative phase diffuses in phase space, leading to a coherent growth of the nonlinear generated fields according to $E_{nl} \propto \sqrt{N}$.